Journal of Nanobiotechnology

RESEARCH

Open Access

Engineered endoplasmic reticulum-targeting nanodrugs with Piezo1 inhibition and promotion of cell uptake for subarachnoid hemorrhage inflammation repair

Xiaojian Zhang[1,2,3†], Enyan Jiang[1,2,3†], Wangyang Fu[1,2,3], Yuanyuan Wang[4,5], Yiping Wang[1,2,3], Zhen Fang[1,2,3], Zichen Zhang[1,2,3], Jiajia Duan[1,2,3], Jia Zeng[1,2,3], Yang Yan[1*] and Fei Liu[1,2,3*]

Abstract

Subarachnoid hemorrhage (SAH) is a life-threatening acute hemorrhagic cerebrovascular condition, often presenting with severe headaches caused by intracranial hypertension, which in severe cases can lead to brain herniation. Piezo1 is a mechanosensitive ion channel protein whose mechanical properties are closely linked to central nervous system diseases. In this study, we developed an engineered endoplasmic reticulum membrane-based nanomedicine (CAQKERM@GsMTx4) using HEK293T cells, aimed at targeted delivery to acute hemorrhagic regions, rapid absorption, and precise inhibition of Piezo1 therapy. To ensure optimal targeting and therapeutic efficacy, we fused the CAQK peptide gene to the N-terminus of TRP-PK1, presenting the CAQK peptide on the endoplasmic reticulum membrane, and loaded GsMTx4 into engineered vesicles (EVs) derived from this engineered membrane. Through in vivo and in vitro experiments and multi-omics analysis, we have demonstrated the marked advantages of endoplasmic reticulum membrane vesicles over cell membrane-based vesicles. CAQKERM@GsMTx4 successfully inhibits Piezo1 in SAH, helps microglia change from the M1 phenotype to the M2 phenotype, and inhibits inflammatory responses and neuronal damage. Overall, this novel engineered endoplasmic reticulum membrane nanomedicine provides a potential effective strategy for the clinical treatment of subarachnoid hemorrhage.

Keywords Piezo1, Engineered endoplasmic reticulum, Intracranial hypertension, Subarachnoid hemorrhage

†Xiaojian Zhang and Enyan Jiang have contributed equally to this work.

*Correspondence:
Yang Yan
yanliuyuxia@163.com
Fei Liu
liuf235@mail.sysu.edu.cn
Full list of author information is available at the end of the article

Graphical Abstract

Engineered endoplasmic reticulum membrane-based nanomedicine, CAQKERM@GsMTx4, specifically targets hemorrhagic regions in subarachnoid hemorrhage (SAH). By inhibiting the Piezo1 ion channel, it promotes M2 microglial transformation, reducing inflammation and neuronal damage. This innovative approach leverages targeted delivery and precise modulation, offering a promising strategy for SAH treatment in both in vitro and in vivo models.

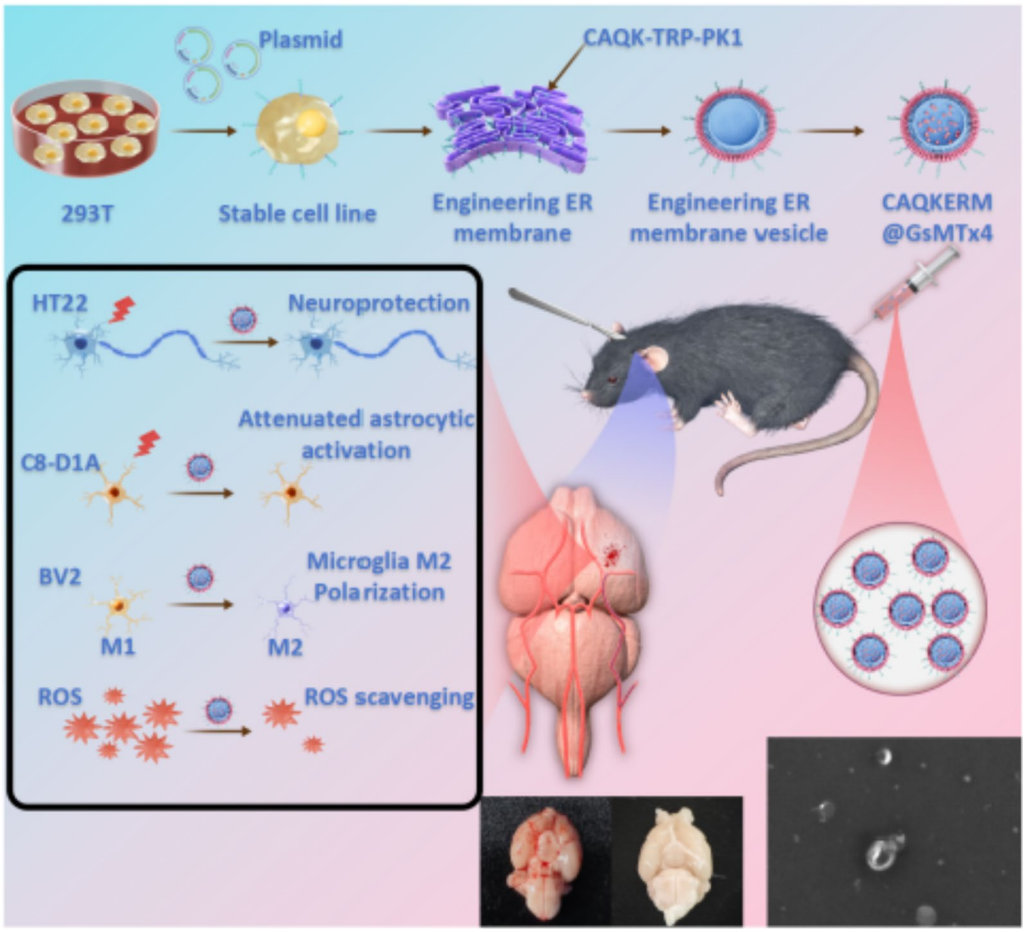

Introduction

Subarachnoid hemorrhage (SAH) refers to a condition in which blood leaks into the subarachnoid space due to the rupture of intracranial vessels. This condition is a common neurosurgical emergency, accounting for approximately 10% of all acute stroke cases [1–3]. The primary clinical symptom in SAH patients is headache, and the pathophysiological process involves the leakage of blood into the cranium, leading to increased intracranial volume and a subsequent rise in intracranial pressure [4]. Early brain injury (EBI) within the first 72 h post-SAH onset is a major determinant of poor prognosis [5, 6]. Researchers have elucidated the potential pathological mechanisms associated with early brain injury (EBI), which include the release of toxic substances such as hemoglobin, thrombin, and iron following the infiltration of blood into the intracranial space, elevated intracranial pressure, and oxidative stress. These factors ultimately result in blood–brain barrier disruption, brain edema, and neuronal cell death. In particular, neuroinflammation related to EBI is a key part of SAH and is seen as a golden phase for therapeutic action [7].Therefore, targeting SAH-related neuroinflammation during EBI could potentially improve neurological outcomes.

Piezo1 is a mechanosensitive ion channel protein that converts extracellular mechanical stimuli into intracellular electrical signals [8]. Multiple studies have shown that inhibiting Piezo1 can mitigate demyelination,

reduce apoptosis in astrocytes and neurons, and modulate the immune response of microglia, thus exerting neuroprotective effects [9–11]. Research has indicated that Piezo1 inhibition can alleviate demyelination caused by hemorrhage by reducing oligodendrocyte and astrocyte apoptosis [9]. Moreover, studies have found that in Piezo1-deficient microglia, the ability to migrate towards amyloid-β is enhanced, and the production of pro-inflammatory cytokines under lipopolysaccharide stimulation is decreased [10]. Aligning with our previous research, intracranial hypertension activated Piezo1, leading to the activation of the Hippo pathway and the induction of neuronal apoptosis, while Piezo1 inhibition attenuates neuronal apoptosis and improves neurological deficits following subarachnoid hemorrhage [11]. Collectively, Piezo1's mechanosensitive properties are closely associated to central nervous system diseases. GsMTx4, an inhibitor of Piezo1, has been shown to effectively block the activation of this ion channel in various experimental models [8, 12]. By inhibiting Piezo1, GsMTx4 prevents the abnormal influx of calcium ions and suppresses the activation of inflammatory cascades, particularly the activation of the M1 phenotype of microglia, which is a key factor in the neuroinflammation observed in subarachnoid hemorrhage (SAH) [9, 10, 13]. In addition to these effects, GsMTx4 has also been reported to reduce apoptosis and oxidative stress, thereby alleviating neuronal damage, promoting neuronal survival, and improving neurological function [11, 14, 15]. These mechanisms suggest that GsMTx4 may serve as a therapeutic agent for mitigating the adverse effects of SAH and other neuroinflammatory diseases. However, due to the widespread expression of Piezo1 channels in cells and the non-specificity of GsMTx4 [12], off-target effects related to Piezo1 inhibition pose a significant challenge that needs to be addressed [14]. More targeted study is needed to improve the effectiveness of therapies and lower the negative effects of off-target effects.

Recent researches in the field of targeted drug delivery have highlighted peptide compounds for their ability to specifically recognize damaged tissues and precisely deliver therapeutic agents and diagnostics to targeted regions [16, 17]. For example, the CAQK peptide (with the amino acid sequence cysteine-alanine-glutamine-lysine) is identified through in vivo phage display screening and found to specifically target brain and neural injury sites [18]. TRP-PK1 is a man-made peptide that comes from the fourth transmembrane domain of the TRPV4 channel. It can attach to the phospholipid bilayers of cell and organelle membranes [19–21]. Therefore, the CAQK peptide can be attached to the surface of made engineered artificial vesicles (EVs) through TRP-PK1. This makes it easier for the EVs to find and attach to brain injury sites. The endoplasmic reticulum membrane (ER membrane, EM), being the largest component of the intracellular membrane system, has not yet been fully explored or developed for use in biomimetic drug delivery systems. Certain proteins expressed in the EM play key roles in facilitating cellular uptake of nanoparticles [22, 23]. Studies have shown that SNARE proteins expressed in the EM can mediate the transport of cholesterol or lipids, rapidly triggering membrane fusion events [24, 25]. Moreover, the endoplasmic reticulum membrane (EM) is enriched with regulatory proteins such as GPX8, which can synergistically enhance the repair effects of therapeutic agents [26]. In addition, compared to exosomes, EM-derived nanovesicles exhibit more uniform size, functional characteristics, and higher yield, while also mitigating the interference of natural heterogeneity on targeting efficiency [22]. Furthermore, EM can be engineered for active targeting and multifunctional therapy, further improving the precision of drug delivery. Studies have shown that the ER membrane decoration on nanoplexes can effectively transport siRNA through the endosome-Golgi-ER pathway, evading lysosomal degradation and enhancing the silencing effects of siRNA [23]. This provides strong evidence for the application of EM in drug delivery.

Considering these factors, the aim of this study was to propose a strategy for constructing an engineered endoplasmic reticulum membrane vesicle drug delivery platform and to explore its potential application in the treatment of subarachnoid hemorrhage. HEK293T cells expressing CAQK-TRP-PK1 were used to successfully create CAQK peptide-modified engineered artificial endoplasmic reticulum membrane vesicles (CAQKERM@EVs). Their effectiveness as a drug delivery platform, especially for targeting brain haemorrhage sites, was confirmed. We also made CAQKERM@GsMTx4 by cleaning the endoplasmic reticulum of HEK293T cells that expressed the CAQK-TRP-PK1 fusion peptide and adding GsMTx4 by extrusion (Fig. 1). We then did physical and biological tests on the system to make sure it worked well. Through a series of experiments, including cell proliferation assays, cellular uptake analysis, and Piezo1 flow cytometry, the significant advantages of the ER membrane as a drug carrier in cellular uptake was confirmed. Additionally, utilizing a SAH mouse model in vivo, we demonstrated that CAQKERM@GsMTx4 effectively targeted the injury region, modulated the immune response of the injury microenvironment, and exhibited neuroprotective effects. The findings suggested that this nanodelivery

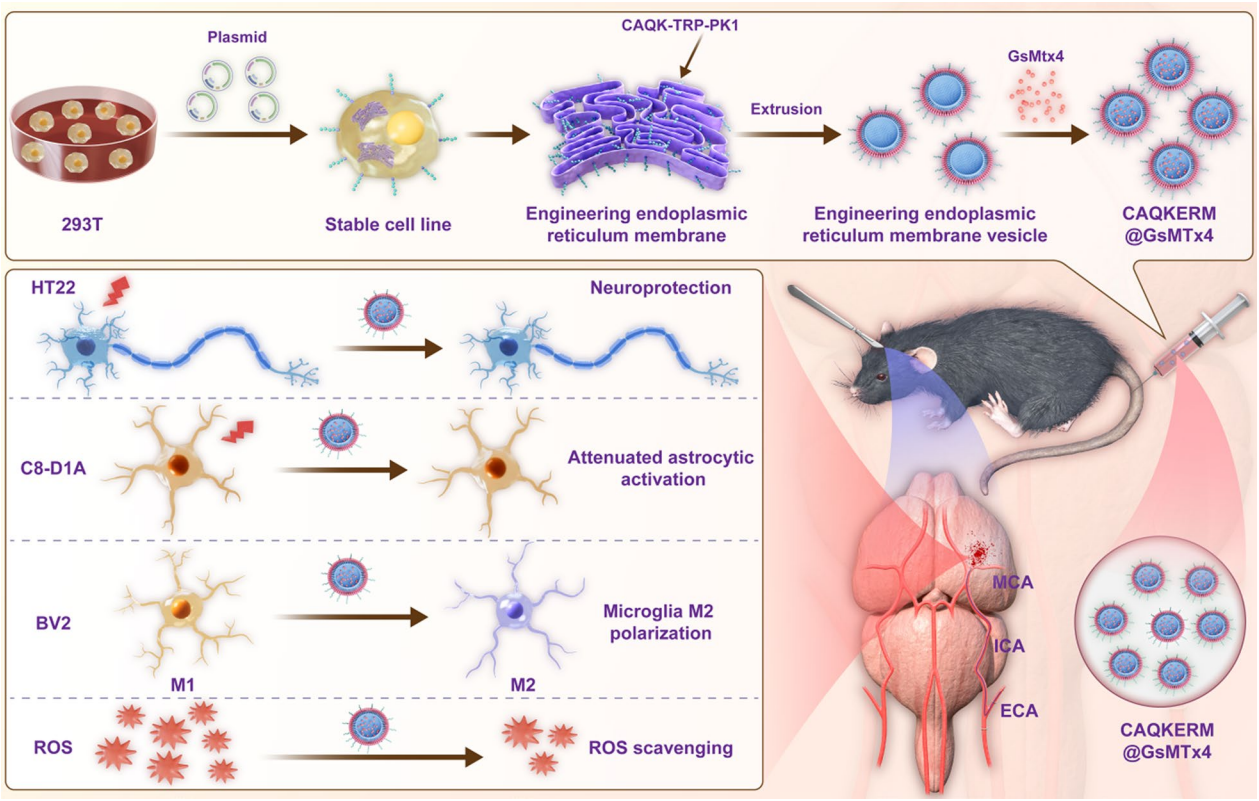

Fig. 1 Schematic illustration of the preparation process for CAQK-incorporated and GsMTx4-loaded engineered endoplasmic reticulum vesicles (CAQKERM@GsMTx4) and th targeted drug delivery for subarachnoid hemorrhage (SAH)

platform hold significant potential for the treatment of brain hemorrhage injuries. Furthermore, the plasticity of the engineered endoplasmic reticulum membrane allows it to incorporate various targeting ligands via TRP-PK1 fusion peptides and to encapsulate a wide range of drugs, offering a novel drug delivery strategy for precision-targeted therapies in other diseases.

Experimental section

Materials, cell culture, and animals

GsMTx4 (HY-P1410A) was sourced from MCE (Guangzhou, China). Hemin solution (0.5 mg/mL, H8132) was provided by Solarbio Life Sciences (Beijing, China). IR780 dye was supplied by Macklin (Guangzhou, China). DiI and DiO dyes were obtained from ThermoFisher (Guangzhou, China). Antibodies targeting GRP94 (14700-1-AP), UNC93B1 (28359-1-AP), and VAMP3 (10702-1-AP) were purchased from Proteintech (Wuhan, China), as well as antibodies against Iba1 (66827-1-Ig), NeuN (66836-1-Ig), and GAFP (60190-1-Ig). DYKDDDDK Tag Recombinant Rabbit Monoclonal Antibody (8H8L17) and Alexa Fluor™ Plus 488, anti-Mouse IgG (A-21202), were obtained from Invitrogen (Shenzhen, China). Anti-Piezo1 antibody (NBP1-78446) was acquired from Novus (Zhuhai, China). HT22, C8-D1A, BV2, and HEK293T cell lines were sourced from icell (Guangzhou, China). All cells were cultured in Dulbecco's Modified Eagle Medium (DMEM) (GIBCO, Guangzhou, China), supplemented with 10% fetal bovine serum (Procell, Guangzhou, China) and 100 U·mL−1 penicillin–streptomycin solution (Procell, Guangzhou, China), at 37 °C under a 5% CO_2 atmosphere. ELISA kits for ARG1, IL6, IL1β, TNF-α, IL10, and TGF-β were supplied by Genkern (Guangzhou, China). The IL4 ELISA kit was provided by Multi Science (Guangzhou, China), while the INOS ELISA kit came from CUSABIO (Wuhan, China). BestBio (Guangzhou, China) is where the ROS test kit was bought. The Animal Care and Use Committee of the Fifth Affiliated Hospital of Sun Yat-Sen University made sure that all animal tests were done according to their rules.

Construction of the CAQK-TRP-PK1 plasmid and transfection

The coding sequence for the CAQK peptide was joined with pieces of TRP-PK1 and put into the pCDH-CMV lentiviral vector to make the pCDH-CAQK-TRP-PK1-flag plasmid. The transfection into HEK293T cells was carried out with polyethylenimine. In short, 2 μg of plasmid and 4 μL of polyethylenimine were mixed together in Opti-MEM™ (Gibco, USA), incubated for 5 min, followed by an additional 15 min before adding the mixture to the cells.

Endoplasmic reticulum (ER) membrane isolation

ER membrane extraction was carried out using a BestBio isolation kit (BB-314542). In short, 1×10^9 CAQK cells were washed with PBS and resuspended in hypotonic extraction buffer (EGTA, HEPES, sucrose, and potassium chloride). After centrifugation, the cells were homogenized in isotonic buffer using a Dounce homogenizer. The supernatant underwent further centrifugation steps, followed by the addition of calcium chloride. The final ER membrane precipitate was stored at −80 °C [23].

Cell membrane (CM) extraction

An pressing method was used to get membrane material. Blank and CAQK cells were washed with PBS and then broken up in cold Tris water (pH 7.4) that has protease inhibitors in it. After spinning, the cell pellets were mixed again, sonicated, and the CM was collected. The BCA method was used to measure the amount of protein in the membrane, and the CM was kept at −80 °C [27].

Characterization of ER membrane functional proteins

Western blot analysis was used to assess protein profiles of EV's, CAQK@EVs, and CAQKERM@EVs. Proteins were separated by SDS-PAGE, transferred onto PVDF membranes, and probed with antibodies against GRP94, UNC93B, and VAMP3. The analysis was performed using the EvosepOne liquid chromatography system coupled with the ZenoTOF 7600 mass spectrometer, with data acquisition conducted on the ZenoTOF 7600 [28].

Loading GsMTx4 into nanovesicles

GsMTx4 (15 μg) was mixed with vesicles derived from the plasma membrane and forced through a 200 nm polycarbonate membrane using an Avanti mini extruder. The 50 μL solution of nanovesicles containing GsMTx4 was then diluted to 1 mL with DMSO to dissolve the vesicles. The specific absorption peak of GsMTx4 at 204 nm was assessed using spectrophotometry, and the concentration of GsMTx4 in each group was calculated based on the absorbance values. The amount of loaded GsMTx4 was calculated using the following equation: $WGSMtx4/WEVs\times100\%$.

Nanoparticle tracking analysis (NTA)

A NanoSight NS300 (Malvern Instruments, UK) was used to measure the concentration and size distribution of nanovesicles. NTA 3.0 software was used to process the results.

Transmission electron microscopy (TEM)

The morphology of nanovesicle was quantified by transmission electron microscopy (TEM). Nanovesicles were negatively stained with 2% uranyl acetate, followed by imaging at 120 kV.

CAQK-TRP-PK1-Flag expression by flow cytometry

HEK293T cells transfected with the CAQK-TRP-PK1-Flag plasmid were stained with a DYKDDDDK-tagged antibody (Invitrogen) to assess Piezo1 expression using flow cytometry.

Pressure and hemin application system

A pressure apparatus was designed to simulate intracranial hypertension. The apparatus consists of a cylindrical structure with a sealed lid, featuring both an air inlet and an outlet (Fig. 3A). When a gas mixture (95% air and 5% CO_2) is introduced through the inlet, the internal pressure increases. The main difference between this pressure device and a standard incubator is the applied pressure. To create a model of intracranial hypertensive hemorrhage, various neuronal cell types were incubated with hemin (60 μM) in the device. The pressure level was preset as the starting condition, and readings were taken every 3 h to ensure pressure stability.

Piezo1 expression by flow cytometry

After treatment, HT22, BV2, and C8-D1A cells were stained with a Piezo1 antibody (Novus Biologicals), followed by a secondary antibody (Alexa Fluor 488). Flow cytometry was used to evaluate Piezo1 expression.

In vivo nanovesicle targeting of subarachnoid hemorrhage (SAH)

Nanovesicles labeled with the fluorescent dye IR780 were injected into SAH mice. After 24 h, brain and other organ imaging was performed using an IVIS Lumina Series III, with radiant efficiency data processed by Living Image 3.1 software.

Subarachnoid hemorrhage (SAH) mouse model

Mice were put to sleep by injecting 50 mg/kg of sodium pentobarbital into their abdomens. The intravascular

perforation method was used to create a model of a subarachnoid haemorrhage (SAH). A 5–0 proline suture was introduced into the intracranial space through the left external carotid artery into the internal carotid artery. In the group that didn't have surgery, the thread was put into the internal carotid artery without starting SAH. They were then put in an incubator at 33 °C for 24 or 72 h [29].

Modified Garcia scale

The modified Garcia scale includes six criteria, with a total score ranging from 3 to 18 [30].

Criterion 1: The mouse is observed in a cage for 5 min to assess its movement. Scoring: 3 points if the mouse moves freely and explores at least three walls; 2 points if it stands still but reaches at least one wall; 1 point if it remains stationary with minimal limb movement; 0 points if no movement is observed.

Criterion 2: The mouse is suspended by its tail to assess limb movement symmetry. Scoring: 3 points for symmetrical limb extension; 2 points if the left limbs extend less or slower than the right; 1 point for minimal left limb movement; 0 points if the left forelimb is immobile.

Criterion 3: The mouse is held by its tail with its forelimbs placed on a table edge to observe climbing. Scoring: 3 points for symmetric forelimb extension; 2 points for impaired left limb extension or climbing difficulty; 1 point for minimal left forelimb movement; 0 points if the left forelimb is immobile.

Criterion 4: The mouse is placed on the wire cage wall to assess its climbing and grasping ability. Scoring: 3 points for normal climbing and gripping; 2 points for impaired left-side grasping; 1 point if the mouse cannot climb or continuously spins when the tail is lifted.

Criterion 5: Somatosensory response is tested by touching both sides of the mouse with a blunt probe. Scoring: 3 points if the mouse reacts equally to both sides and escapes; 2 points if the response to left-side stimulation is slower; 1 point if there is no response to left-side stimulation.

Criterion 6: Whisker response is tested by stroking the whiskers on both sides with a blunt probe, avoiding the visual field. Scoring: 3 points if the mouse reacts equally to both sides; 2 points if the left-side response is slower; 1 point if there is no response to left-side stimulation.

Each mouse is evaluated in a double-blind manner, and the total score is the sum of the six criteria, ranging from 3 (lowest) to 18 (highest) points.

Balance beam test

In the balance beam test, mice are placed on a 15-mm wide beam, elevated 0.5 m. This test is part of the modified neurological severity score (mNSS), used to assess balance. A higher mNSS score indicates more severe impairment. The 6-point scale is as follows:

0: Mouse maintains stable balance on the beam for over 60 s.
1: Mouse grips one side of the beam.
2: Mouse grips the beam, but one limb slips off.
3: Mouse grips the beam, but two limbs slip or it spins to maintain balance for over 60 s.
4: Mouse attempts to balance but falls within 40 s.
5: Mouse attempts to balance but falls within 20 s.
6: Mouse falls with no attempt to balance, or hangs on the beam for less than 20 s.

Morris water maze assay

This assay assessed spatial learning and memory in SAH mice from day 3 to day 7 post-treatment. Mice were placed in a pool, and the time to reach the escape platform was recorded. On day 7, memory tests were conducted by removing the platform and recording swimming patterns.

Open field test

At 7 days post-SAH, motor function was assessed by placing mice in an open-field box, with movement and activity tracked using a video system (ANYmaze, Stoelting, IL, USA).

(See figure on next page.)

Fig. 2 Characterization of CAQKERM@GsMTx4. **A** Schematic illustration of CAQKERM@GsMTx4 preparation. **B** Flow cytometry analysis showing Flag-tagged Blank and CAQK expression (Flag) in transfected and non-transfected HEK293T cells. **C** Quantification of the mean fluorescence intensity in **B**. **D** Confocal microscope pictures of CAQK showing up on the cell membrane of HEK293T cells that had Flag-tagged CAQK-expressing plasmid (CAQK) and Blank plasmid (Blank) added to them **E** Confocal microscopy images showing colocalization of CAQK (Alexa Fluor™ 488-conjugated) with markers for the endoplasmic reticulum, mitochondria, and lysosomes in CAQK-expressing HEK293T cells. **F** Standard curve for detecting GsMTx4 using a spectrophotometer. **G** GsMTx4 loading efficiency in different vesicles ($n = 3$). **H** Morphological characterization of EV's, CAQK@EVs, CAQKERM@EVs, Blank@GsMTx4, CAQK@GsMTx4, and CAQKERM@GsMTx4 by TEM. Scale bar: 200 nm. **I** Size distribution analysis of EV's, CAQK@EVs, CAQKERM@EVs, Blank@GsMTx4, CAQK@GsMTx4, and CAQKERM@GsMTx4 by nanoparticle tracking analysis. **J** SDS-PAGE and **K** Western blot analysis of membrane proteins

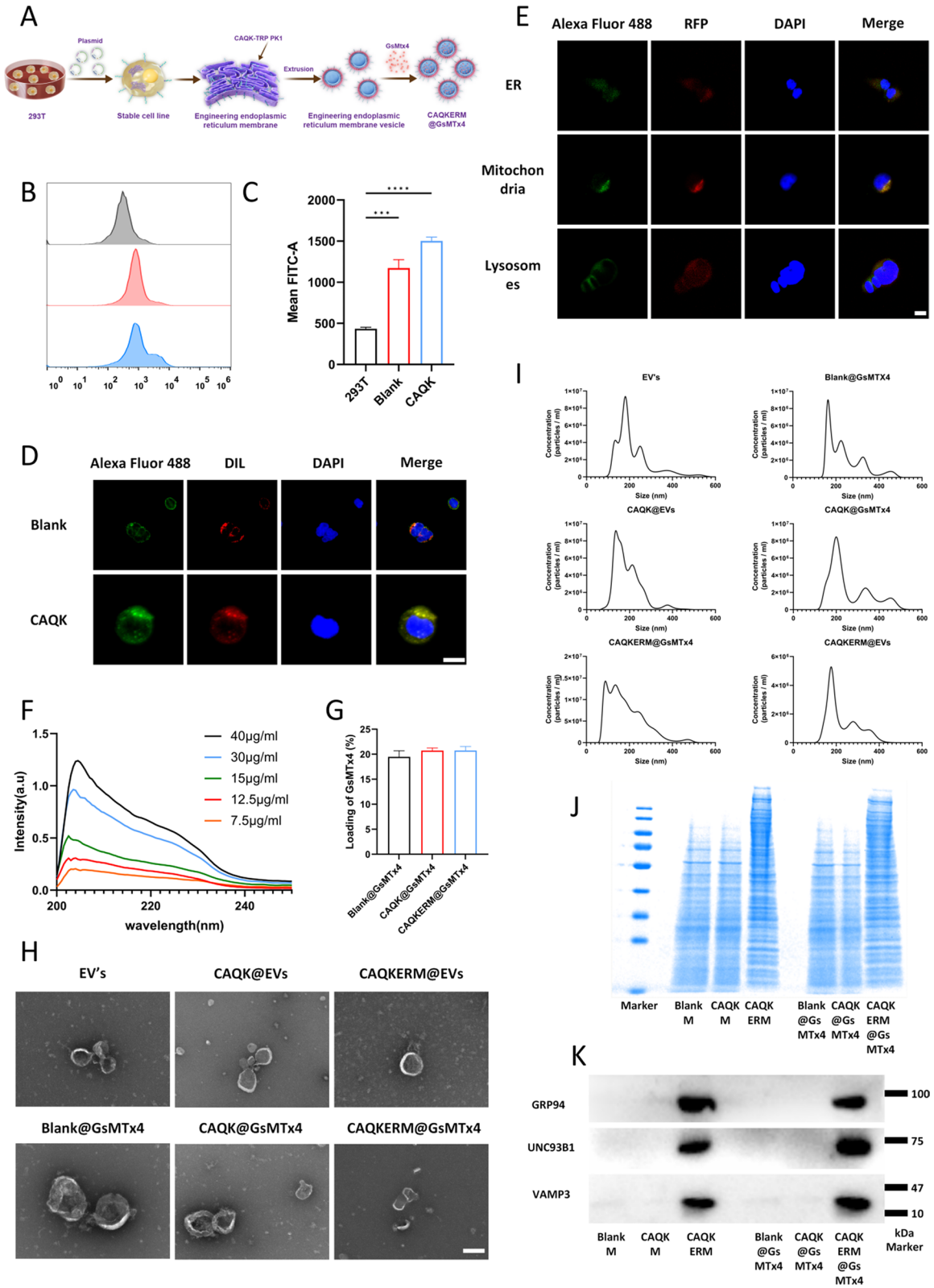

Fig. 2 (See legend on previous page.)

Immunofluorescence staining of mouse brain tissue

Following PBS and paraformaldehyde perfusion, brain tissue was sectioned (20 μm) and blocked with donkey serum. Sections were incubated with primary antibodies against Iba1, NeuN, and GFAP, followed by fluorescent secondary antibodies. DAPI was used for nuclear staining, and imaging was performed using a digital pathology scanner (P250 FLASH).

RNA sequencing

Total RNA was extracted from SAH brain tissue, followed by RNA sequencing at Personalbio (Shanghai, China). Data analysis was conducted using hiplot online platform.

Statistical analysis

The numbers were shown as mean ± S.D. or mean ± S.E.M. The Student's *t* test was used to compare two groups, and one-way ANOVA followed by Tukey's post-hoc test was used to compare more than two groups. The study was done with GraphPad Prism 9.5.0, and a value of $p < 0.05$ was thought to be statistically significant.

Results and discussion

Preparation and characterization of engineered endoplasmic reticulum-targeting nanodrugs, CAQKERM@GsMTx4

To develop an efficient targeted biomimetic nanodrug for the treatment of subarachnoid hemorrhage (SAH), we adopted the following strategy: CAQK-TRP-PK1 fusion peptides were displayed on the surface of nanovesicles prepared from the endoplasmic reticulum (ER) membrane, while the vesicle interior encapsulated the piezo1 inhibitor GsMTx4 (CAQKERM@GsMTx4). Initially, we constructed a DNA clone that enabled the effective expression of the CAQK-TRP-PK1 fusion peptide (Fig. S1). This construct was transfected into HEK293T cells, facilitating the expression and display of the CAQK-TRP-PK1 fusion peptide on both the plasma membrane and ER membrane. Vesicles were prepared by co-extruding the ER membrane and GsMTx4 through a liposome extruder, yielding artificial ER membrane vesicles loaded with GsMTx4 and displaying the CAQK-TRP-PK1 fusion peptide (CAQKERM@GsMTx4), designed to target hemorrhagic injury sites in the brain (Fig. 2A).

To verify this approach, a pCDH-CMV-MCS-EF1-Puro vector was engineered to express the CAQK targeting peptide sequence fused to TRP-PK1 at the N-terminus, with a flag tag on the C-terminus (pCDH-CAQK-TRP-PK1-flag plasmid). This construct has been previously shown to assist in integration into lipid bilayers. HEK293T cells transfected with the pCDH-CAQK-TRP-PK1-flag plasmid exhibited high levels of CAQK-TRP-PK1-Flag bound to the cell membrane, as confirmed by flow cytometry analysis (Fig. 2B, C). Confocal imaging showed that CAQK-TRP-PK1-Flag was found on the plasma membrane (Fig. 2D) as well as on the membranes of organelles, mainly the ER and mitochondrial membranes (Fig. 2E).

Previous studies have shown that functional proteins on the ER membrane play a critical role in enhancing cellular uptake and modulating intracellular protein levels. Therefore, we utilized a liposome extruder to prepare artificial ER membrane vesicles and drug-loaded vesicles from HEK293T cells expressing the CAQK-TRP-PK1 fusion protein. As controls, we prepared engineered artificial vesicles (CAQK@EVs, EV's) and GsMTx4-loaded vesicles (CAQK@GsMTx4, Blank@GsMTx4) from cell membranes derived from HEK293T cells transfected with either pCDH-CAQK-TRP-PK1-flag plasmid or pCDH-TRP-PK1-flag plasmid. Freshly prepared EVs encapsulating GsMTx4 were quantified using UV spectrophotometry, with the characteristic absorbance peak of GsMTx4 identified at 204 nm. The standard curve was used to figure out the concentration of GsMTx4 when the GsMTx4 concentration was between 7.5 and 40 μg/mL (Fig. 2F, G). Transmission electron microscopy (TEM) pictures showed that all vesicles, including drug-loaded vesicles, had a spherical shape and a lipid membrane, which were similar with naturally released exosomes (Fig. 2H). Dynamic light scattering (DLS) analysis showed that the largest particles in the vesicles and drug-loaded vesicles were about 220 nm in diameter, which was about the same size as naturally released exosomes (Fig. 2I). We did a study

(See figure on next page.)

Fig. 3 The treatment effectiveness and targeting efficiency of CAQKERM@GsMTx4 in vitro. **A** A drawing of the pressure device. **B** Measuring the amount of M1 and M2 macrophage markers present in BV2 cells that are activated by blood and pressure. The amount of ROS in the fluid around BV2 cells that are activated by blood and pressure (**C**). Findings of **D** cytokines that cause inflammation and **E** cytokines that stop inflammation in the fluid around BV2 cells that have been activated by blood and pressure. **F**–**H** Confocal microscopy images and **I** fluorescence density analysis of DiI-labeled EV's, CAQK@EVs, or CAQKERM@EVs uptake by C8-D1A, BV2, and HT22 cells after 2 h of incubation. Scale bar: 10 μm. Flow cytometry analysis of Piezo1 protein expression in **J** C8-D1A, **K** BV2, and **L** HT22 cells. For all experiments, data are presented as mean ± SD for $n = 3$ biological replicates. * $p < 0.05$, ** $p < 0.01$, or *** $p < 0.001$

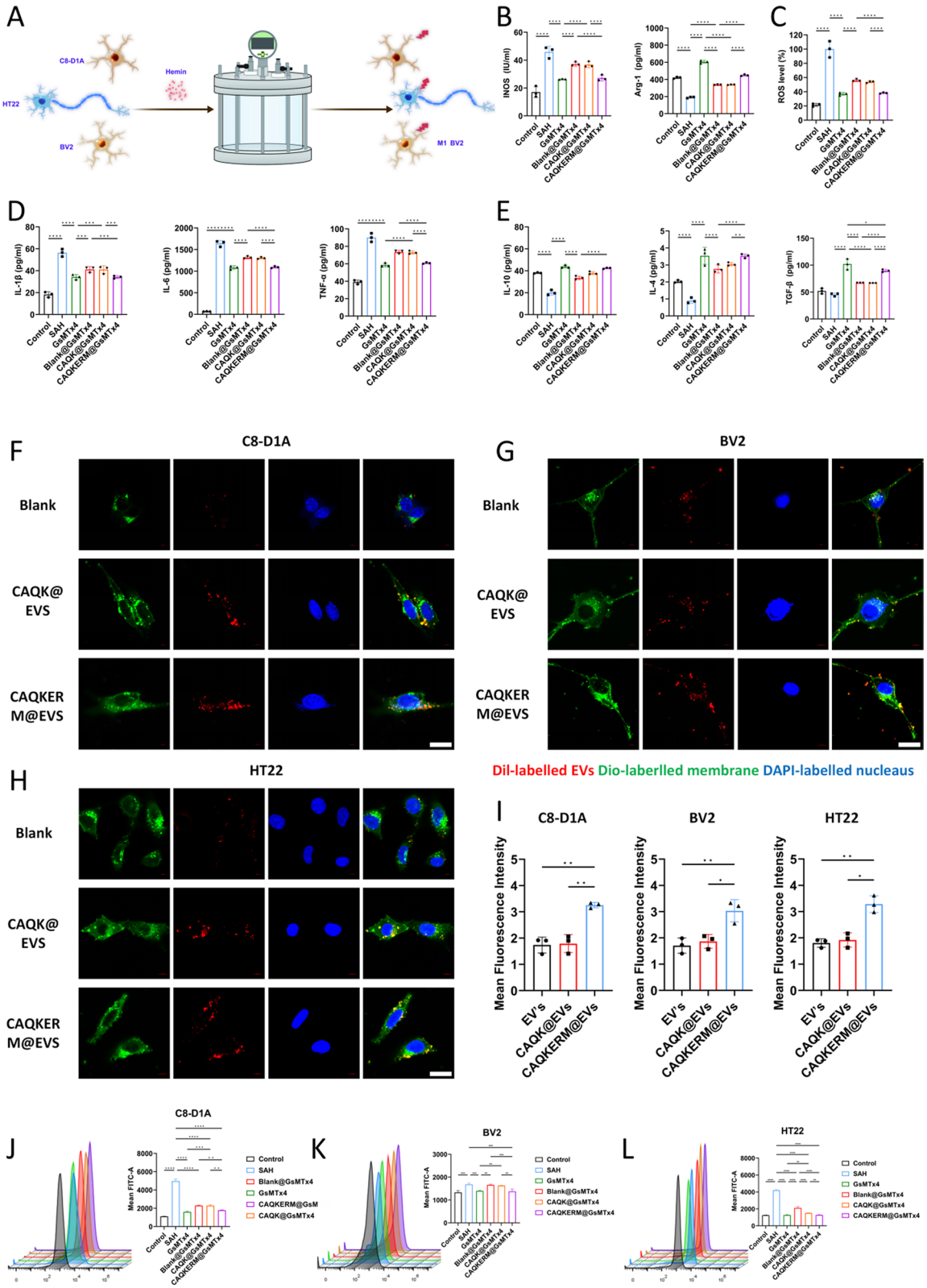

Fig. 3 (See legend on previous page.)

using SDS-PAGE and western blot to look at the protein parts in the vesicles and drug-loaded vesicles. The results showed that the main protein parts of CAQKERM were still there in CAQKERM@GsMTx4, mainly UNC93B31 and GRP94 [31, 32], which are important ER membrane markers (Fig. 2K). Moreover, vesicle-associated membrane protein 3 (VAMP3) was found in both CAQKERM and CAQKERM@GsMTx4. VAMP3 was a member of the SNARE family and was involved in the movement of vesicles. The protein components retained in Blank@GsMTx4 and CAQK@GsMTx4 exhibited electrophoretic bands consistent with those of the plasma membrane [24].

In this study, proteomic techniques were employed to comparatively analyze proteins present in Blank cell membranes (BlankM), CAQK cell membranes (CAQKM), and CAQK endoplasmic reticulum membranes (CAQKERM). The results showed that compared with BlankM and CAQKM, CAQKERM exhibited significantly higher levels of vesicular transport proteins (Fig. S3A–B). HALLMARK, GO, KEGG, and REACTOME enrichment analyses revealed that CAQKERM had an upregulation of proteins in comparison with the control groups (Fig. S3C–D), and functional annotation based on the GO database (Fig. S4A–B) indicated that these upregulated proteins were classified into three main categories: "Cellular Component (CC)," "Molecular Function (MF)," and "Biological Process (BP)," suggesting that CAQKERM is enriched with functional proteins. Further enrichment analysis demonstrated that CAQKERM is rich in regulatory proteins capable of modulating various biological functions, including "Transport vesicle," "Regulation of metabolic process," "Metal ion transmembrane transporter activity," and "Peptide binding". Additionally, KEGG enrichment analysis explored the pathways involved in the upregulated proteins (Fig. S4C–D), showing associations with the endocrine system ("PPAR signaling pathway," "Adipocytokine signaling pathway"), protein folding and degradation ("Protein export," "SNARE interactions in vesicular transport"), signal transduction ("Wnt signaling pathway," "MAPK signaling pathway"), and lipid metabolism ("Glycerophospholipid metabolism," "Steroid biosynthesis," "Biosynthesis of unsaturated fatty acids"). In comparison with BlankM and CAQKM, CAQKERM is enriched with more inflammation-related regulatory proteins, such as GPX8, GRP78, V-ATPase, SIGMAR1, FAM134B, RTN3 and others (Fig. S5A–B) [26, 33–37]. This may contribute to a more synergistic interaction between the drug-loaded delivery system constructed with CAQKERM and the GsMTx4.

Overall, our findings show that CAQKERM was full of functional proteins which played an important role in many physiological processes and signalling pathways. These results elucidated its potential utility as a drug delivery platform.

Immunomodulatory, neuroprotective, ROS scavenging, and cellular uptake of CAQKERM@GsMTx4 in vitro

The mechanism of SAH encompasses excitotoxicity and excessive production of reactive oxygen species (ROS) due to the abrupt bleeding, leading to the death of numerous neurons in the affected area [38]. Damage-associated molecular patterns (DAMPs) released by dying neurons activate microglia, promoting their polarization into the pro-inflammatory M1 phenotype. This leads to the release of pro-inflammatory cytokines, such as TNF-α, IL-1β, and IL-6, which exacerbate neuronal damage and contribute to secondary injury [39–42]. Therefore, effectively repairing damaged neurons, reducing ROS production, and promoting the polarization of microglia toward the anti-inflammatory M2 phenotype are anticipated to enhance tissue repair and facilitate the recovery of neurological function, offering a substantial therapeutic advantage.

To evaluate the anti-inflammatory effects of CAQKERM@GsMTx4, we developed a pressure-blood infusion device to simulate intracranial hemorrhage conditions (Fig. 3A). Previous studies have shown that intracranial pressure peaks at approximately 15 kPa following SAH in mice. We initially tested the device for air-tightness to ensure the maintenance of a stable hypertensive environment (Fig. S2).

BV2 microglial cells were exposed to stimulation in the device for 24 h, followed by co-incubation with GsMTx4,

(See figure on next page.)

Fig. 4 Targeting capacity of CAQKERM@GsMTx4. **A** In vivo and ex vivo imaging of IR780, Blank@IR780, CAQK@IR780, and CAQKERM@IR780 in the hemorrhagic brain of SAH mice 24 h post-injection. **B** Semi-quantification of IR780, Blank@IR780, CAQK@IR780, and CAQKERM@IR780 in the brain based on IR780 fluorescence intensity. **C** Ex vivo imaging of IR780, Blank@IR780, CAQK@IR780, and CAQKERM@IR780 in the heart, liver, spleen, lungs, and kidneys 24 h post-injection. **D** Semi-quantification of IR780, Blank@IR780, CAQK@IR780, and CAQKERM@IR780 in these organs based on IR780 fluorescence intensity. **E** Time course of in vivo targeting studies. **F**–**H** Colocalization of Flag EVs with different cell types. Brain sections were stained with antibodies for different cell types, followed by secondary antibody (488, green) staining. Nuclei were stained with DAPI (blue). Scale bar: 50 μm. **I**–**K** Fluorescence density analysis. For all experiments, data are presented as mean ± SD for $n = 6$ biological replicates. * $p < 0.05$, ** $p < 0.01$, or *** $p < 0.001$

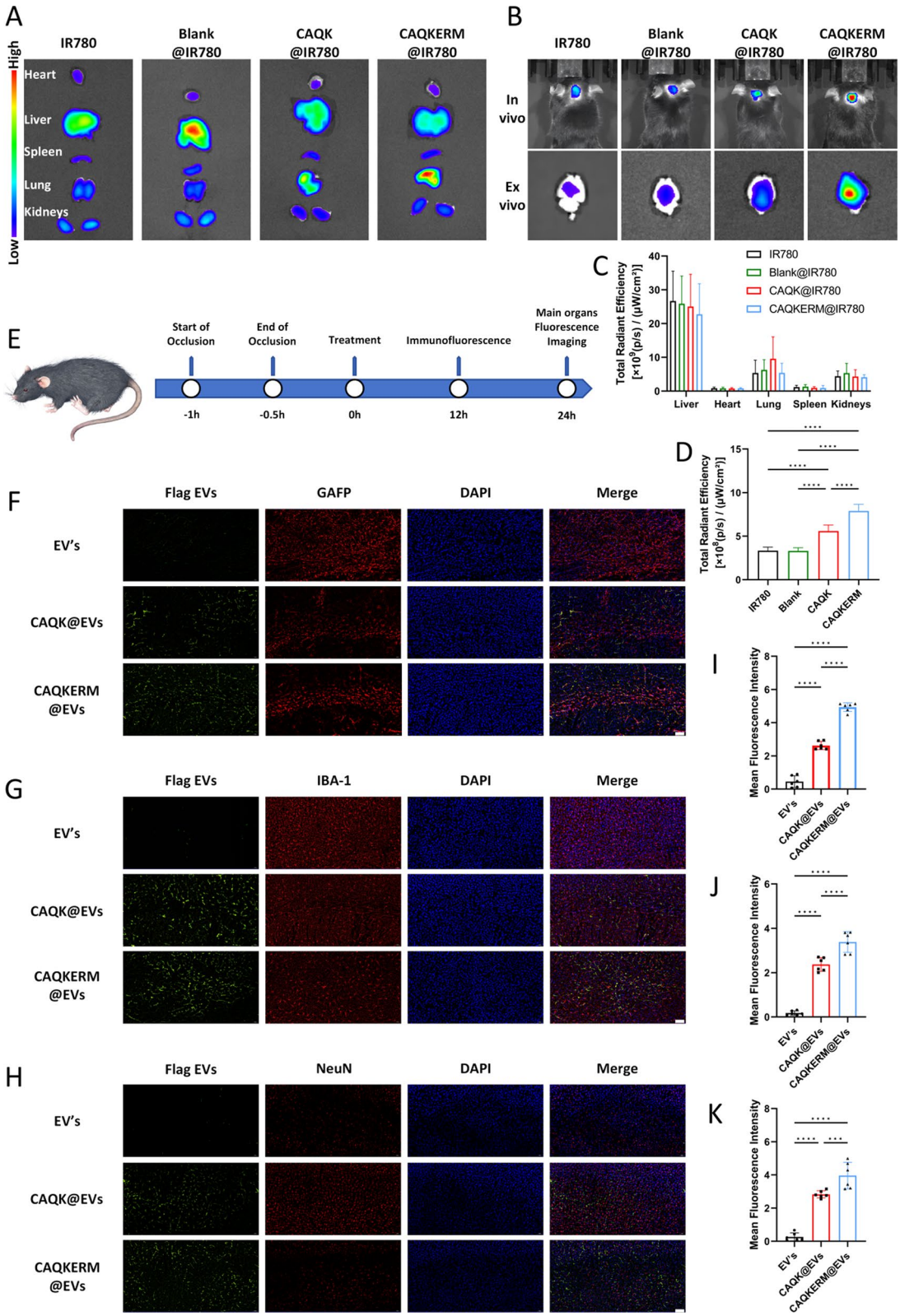

Fig. 4 (See legend on previous page.)

Blank@GsMTx4, CAQK@GsMTx4, or CAQKERM@GsMTx4 for an additional 24 h. Macrophage markers and inflammatory cytokines were subsequently analyzed. Compared to untreated cells, pressure-blood-treated BV2 cells exhibited significantly higher levels of inducible nitric oxide synthase (iNOS), a classical M1 marker (Fig. 3B), along with elevated levels of TNF-α, IL-1β, and IL-6 (Fig. 3D), while the anti-inflammatory cytokine IL-4 was markedly reduced (Fig. 3E). Treatment with the drugs or drug-loaded vesicles significantly lowered the levels of iNOS, ROS, and pro-inflammatory cytokines (Fig. 3B–D). Notably, CAQKERM@GsMTx4 demonstrated anti-inflammatory effects comparable to direct drug administration, significantly upregulating IL-4, IL-10, TGF-β, and the M2 marker Arg-1 [43] (Fig. 3B, E). Cellular uptake capacity is essential for an optimal drug delivery system. To evaluate this, we labeled EV's, CAQK@EVs, and CAQKERM@EVs with 1,1′-dioctadecyl-3,3,3′,3′-tetramethylindocarbocyanine perchlorate (DiI; red fluorescence) and incubated them with C8-D1A, BV2, and HT22 cells that had been pre-treated for 24 h using a pressurized perfusion device. The cells were then incubated for an additional 4 h. Confocal microscopy analysis revealed that DiI-labeled CAQKERM@EVs were highly enriched in cells within the brain hemorrhage model (Fig. 3F–I). These findings indicate that endoplasmic reticulum membrane-based vesicles demonstrate superior uptake efficiency in neural cells following brain hemorrhage injury. Additionally, extended incubation of CAQKERM@EVs with these injured neural cells for 12 and 24 h showed sustained vesicle accumulation in the damaged cells (Figs. S6, S7).

We subsequently investigated the inhibition of Piezo1 in vitro using drug-loaded vesicles. Neuronal cells subjected to various types of damage, simulated by pressure-driven blood perfusion, were treated with the drug-loaded vesicles. Compared to cells exposed to the pressure device alone, treatment with both the drug and drug-loaded vesicles significantly reduced the abnormal activation of Piezo1 induced by the pressure device. Notably, CAQKERM@GsMTx4 produced effects comparable to direct drug administration (Fig. 3J–L). These results suggested that CAQKERM@GsMTx4 mitigated inflammation by inhibiting Piezo1 and CAQKERM@EVs were efficiently absorbed by cells. The combination of these strategies showed great potential for achieving optimal therapeutic outcomes in vivo.

CAQKERM@GsMTx4 efficiently targeted the subarachnoid hemorrhage

To investigate the targeting capability of engineered vesicles for hemorrhagic lesions, vesicles loaded with IR780 (Blank@IR780, CAQK@IR780, and CAQKERM@IR780) were intravenously administered into subarachnoid hemorrhage (SAH) model mice, followed by immunofluorescence staining to observe vesicle infiltration in the infarcted brain tissue (Fig. 4E). As shown in Fig. 4B, fluorescence signals were significantly enhanced in the brain tissue of mice treated with CAQKERM@IR780, with a signal intensity 2.38 times higher than that of the IR780 group (Fig. 4D). No significant differences in biodistribution were observed between the two groups outside of the brain tissue (Fig. 4A, C). The reason for the higher fluorescence intensity in the liver may be due to the natural accumulation of nanovesicles injected intravenously in the liver tissue, which is a common phenomenon in studies of various nanoparticle treatments for diseases.

To further evaluate the uptake of modified vesicles by different types of brain cells, brain tissue sections were stained with antibodies recognizing neurons (NeuN), microglia (IBA1), and astrocytes (GFAP). As illustrated in Fig. 4F–J, the green fluorescence of engineered vesicles colocalized with the magenta fluorescence of NeuN (Fig. 4F), IBA1 (Fig. 4G), and GFAP (Fig. 4H). This indicates that the engineered vesicles were broadly distributed within neurons, microglia, and astrocytes in mouse brain tissue, with high fluorescence intensity observed (Fig. 4I–K). These findings demonstrate that intravenously administered modified vesicles accumulate extensively in the brain parenchyma and subsequently localize to neurons, microglia, and astrocytes.

CAQKERM@GsMTx4 reversed pro-inflammatory microenvironment, enhanced neuroprotection, and ROS scavenging

To evaluate the therapeutic effects of engineered endoplasmic reticulum membrane nanomedicine

(See figure on next page.)

Fig. 5 Therapeutic effects of CAQKERM@GsMTx4 in the SAH brain. **A** Experimental timeline. **B** Representative images of brain ROS levels in sham and SAH mice 24 h post-injury. **C** ROS levels in the right hemisphere of SAH mice 24 h post-treatment. Measurement of **D** pro-inflammatory and **E** anti-inflammatory cytokines in the right hemisphere of SAH mice. **F** Quantification of M1 and M2 macrophage markers in the right hemisphere. **G** Representative fluorescent images of microglia (Iba1), glial scar (GFAP), and neurons (NeuN) in infarct areas across groups 3 days post-treatment. Scale bar: 50 μm. **H** Fluorescence intensity of Iba1, GFAP, and NeuN corresponding to **G**. For all experiments, data are presented as mean ± SD for $n = 6$ biological replicates. * $p < 0.05$, ** $p < 0.01$, or *** $p < 0.001$

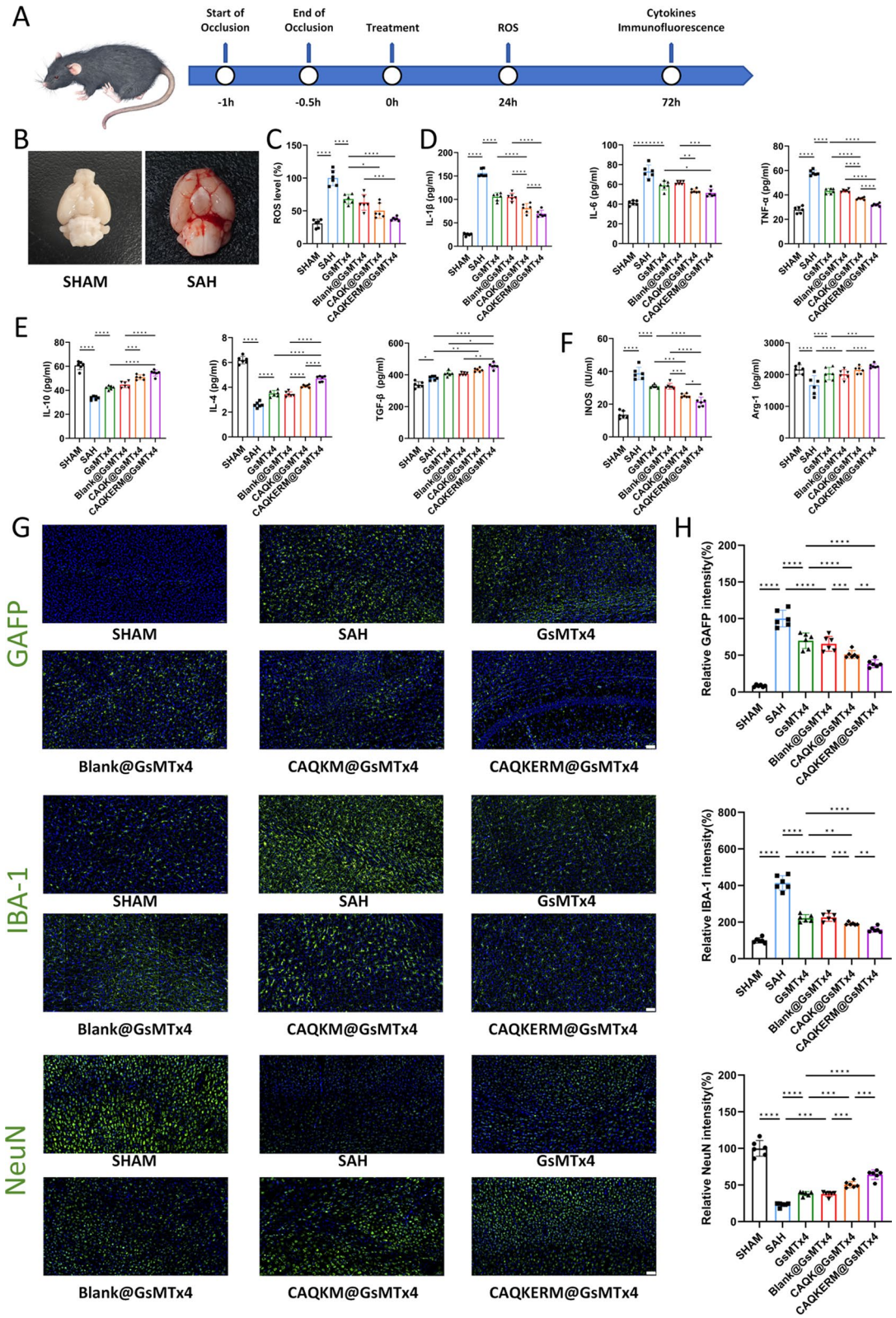

Fig. 5 (See legend on previous page.)

(CAQKERM@GsMTx4), tail vein injections of CAQKERM@GsMTx4 were administered to SAH mice (Fig. 5A). At 72 h post-treatment, protein expression levels of M1 and M2 markers, along with inflammatory cytokines in the right hemisphere of the brain, were assessed (Fig. 5B). As shown in Fig. 6D–F, levels of IL-1β, IL-6, TNF-α (Fig. 5D), and iNOS (Fig. 5F) were significantly reduced in mice treated with CAQKERM@GsMTx4 compared to those treated with GsMTx4, Blank@GsMTx4, or CAQK@GsMTx4. In contrast, levels of IL-10, IL-4, TGF-β (Fig. 5E), and Arg-1 (Fig. 5F) were notably higher. Furthermore, in the right hemisphere, expression of Iba1 (a marker of microglial activation) and GFAP (a marker of astrocyte activation, indicative of CNS pathology) [44, 45] was lower in the CAQKERM@GsMTx4 group (Fig. 5G). Fluorescence quantification revealed that Iba1 and GFAP levels in the CAQKERM@GsMTx4 group were only 38.54% and 38.35%, respectively, compared to the model group (Fig. 5H). These findings indicate that CAQKERM@GsMTx4 provides superior anti-inflammatory effects following SAH.

Additionally, ROS production in the right hemisphere was measured 24 h post-treatment. CAQKERM@GsMTx4 significantly reduced ROS levels (Fig. 5C). The role of CAQKERM@GsMTx4 in preserving tissue in the infarcted region was also assessed. At 72 h post-treatment, tissue staining for the neuronal marker NeuN was conducted. Immunofluorescence analysis demonstrated that CAQKERM@GsMTx4 treatment substantially alleviated tissue damage. Overall, CAQKERM@GsMTx4 exhibited pronounced neuroprotective effects and effectively reduced ROS levels, outperforming GsMTx4, Blank@GsMTx4, and CAQK@GsMTx4. This superior therapeutic outcome is likely attributed to CAQKERM@GsMTx4's enhanced targeting and absorption in the lesion area of the right hemisphere post-hemorrhage. In contrast, GsMTx4 and Blank@GsMTx4 showed lower accumulation (Fig. 4B), and CAQK@GsMTx4 exhibited slower uptake, limiting its efficacy.

CAQKERM@GsMTx4 treatment enhanced post-stroke functional recovery

In vivo behavioral assessments were performed to evaluate the therapeutic efficacy of CAQKERM@GsMTx4 (Fig. 6A). SAH significantly impaired sensorimotor function, as indicated by reduced Garcia scores (Fig. 6B) and diminished performance in the beam balance test (Fig. 6C). Treatment with CAQKERM@GsMTx4 demonstrated potential in promoting neurological recovery (Fig. 6B, C), suggesting its neuroprotective effects on hemorrhagic brain injury. In the open field test (Fig. 6D), mice treated with CAQKERM@GsMTx4 exhibited greater total movement distance (Fig. 6E), speed (Fig. 6F), and activity levels (Fig. 6G) on day 7 post-SAH compared to other treatment groups. These findings indicate that CAQKERM@GsMTx4 effectively improves neurological function in SAH mice.

To further assess learning ability and spatial memory, we conducted the Morris water maze (MWM) test on SAH mice following various treatments. On day 7 post-SAH, representative swimming paths were recorded (Fig. 6H, I), revealing significant impairments in learning and spatial memory in SAH-treated mice. By the final day of the learning phase, the swimming paths showed that SAH mice treated with CAQKERM@GsMTx4 reached the platform via the shortest route (Fig. 6H), indicating reduced neurological damage compared to other groups (Fig. 6J). After platform removal, SAH mice traveled shorter distances and spent less time in the target quadrant compared to sham-operated mice, indicating impaired spatial memory. However, treatment with GsMTx4 and drug-loaded vesicles significantly improved spatial memory, increasing both distance traveled and time spent in the target quadrant (Fig. 6K). Swimming speed remained consistent across groups during the MWM test (Fig. 6K). These results demonstrate that CAQKERM@GsMTx4 contributes to behavioral recovery.

Study on molecular mechanisms

To elucidate the molecular mechanisms underlying the therapeutic effects of CAQKERM@GsMTx4 in treating SAH, we performed whole-genome RNA sequencing on SAH brain tissues 24 h post-treatment. We identified

(See figure on next page.)

Fig. 6 Neurobehavioral recovery of SAH mice. **A** Experimental timeline. Neurological scores assessed by **B** modified Garcia scale and **C** beam balance test at 24 h post-SAH. **D** Representative mouse paths in the open field test. **E**–**G** Open field test measuring disease-related behavioral parameters in SAH mouse models. Representative swimming paths of mice indicating their **H** learning and **I** memory abilities as determined by the Morris water maze test. **J**,**K** Disease-related behavioral parameters measured by the Morris water maze test in SAH mouse models. For all experiments, data are presented as mean ± SD for $n = 6$ biological replicates. * $p < 0.05$, ** $p < 0.01$, or *** $p < 0.001$

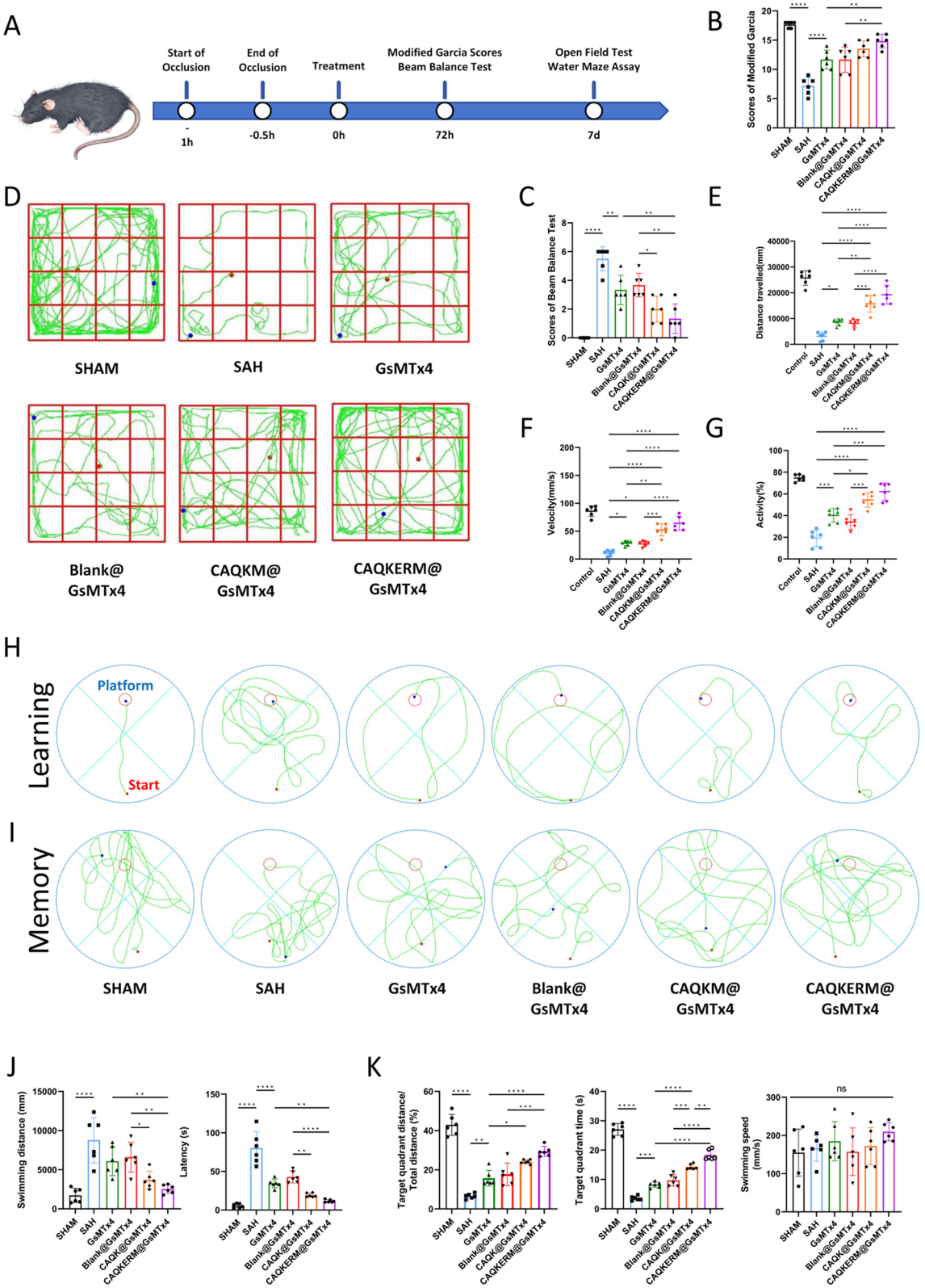

Fig. 6 (See legend on previous page.)

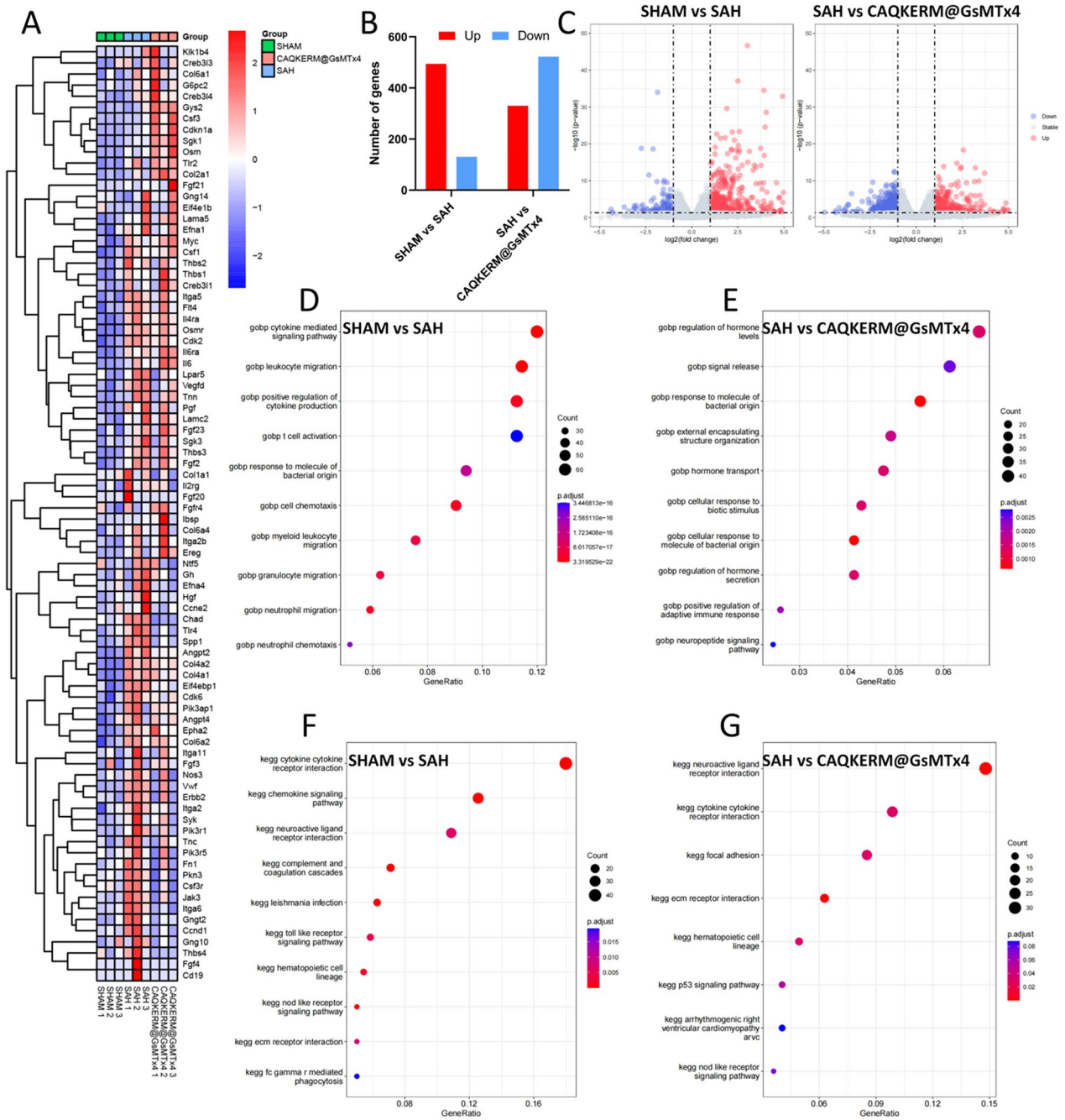

Fig. 7 RNA-seq analysis of SAH brain tissues after different treatments. **A** Heatmap of DEGs clustered after different treatments. **B** Summary of DEGs in SAH brain samples 24 h after different treatments. In **C**, volcano plots of DEGs are used to make different comparisons. **D**,**E** A GOBP enrichment study of pathways in the SAH group and the other treatment groups. **F**,**G** A KEGG pathway study of the pathways that were more active in the treatment groups compared to the SAH group

a total of 17,990 gene transcripts, including 605, 183, and 306 transcripts that were exclusively expressed in the sham, SAH, and CAQKERM@GsMTx4 groups, respectively (Fig. S8). Compared to the SAH group, the sham group exhibited 1407 differentially expressed genes (DEGs), with 759 upregulated genes (red dots) and 648 downregulated genes (blue dots). In the CAQKERM@GsMTx4 group, 852 DEGs were identified, comprising 330 upregulated and 522 downregulated genes (Fig. 7B–C).

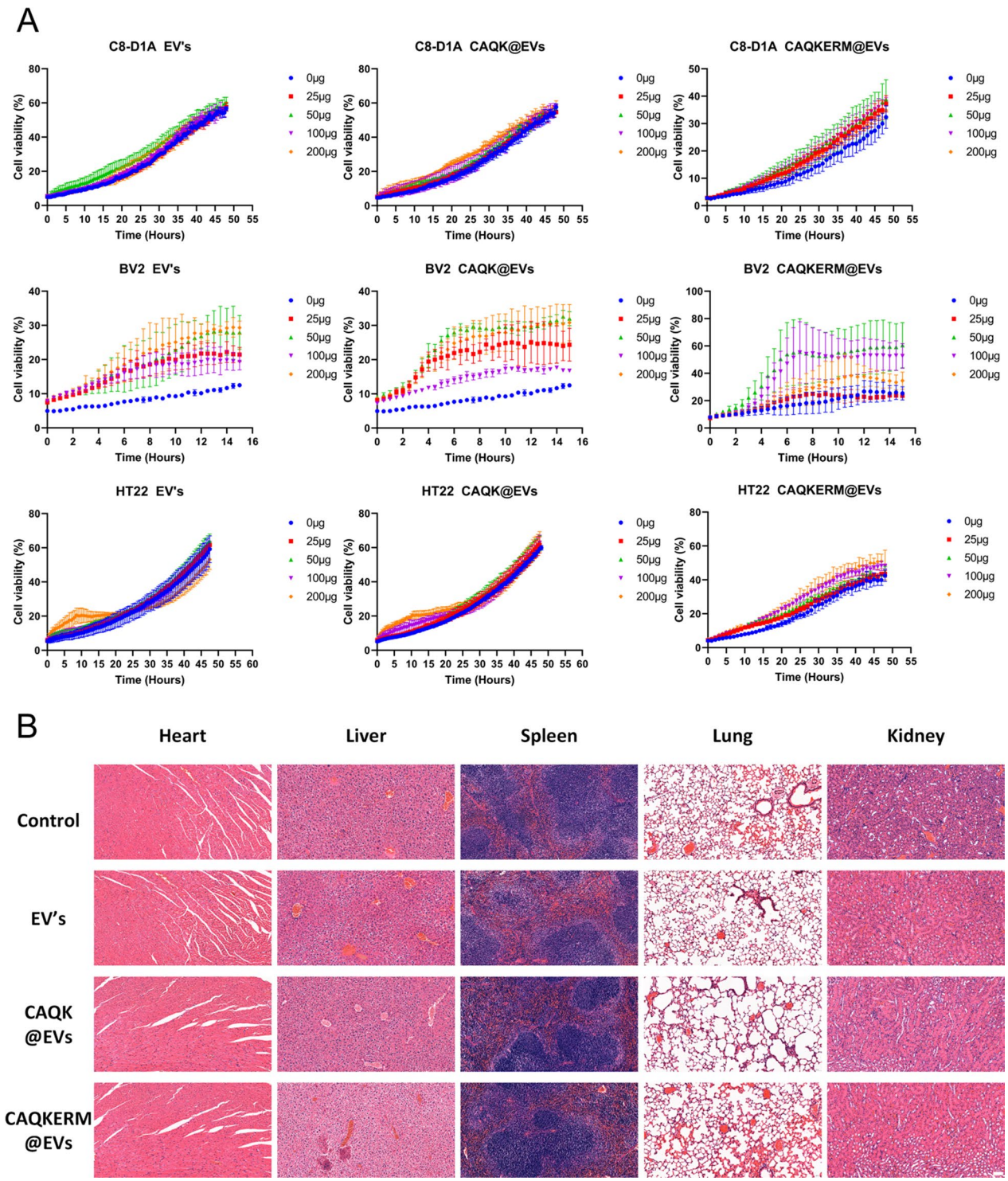

Fig. 8 Safety evaluation. **A** Cell viability assay of C8-D1A, BV2 and HT22, cells treated for 24 h with different dosages (0, 25, 50, 100, 200 μg) of EV's, CAQK@EVs, and CAQKERM@EVs. **B** H&E staining of major organs. Scale bar: 50 μm

Gene Ontology Biological Process (GOBP) analysis (Fig. 7D–E) and cnetplot visualization (Fig. S9) demonstrated that CAQKERM@GsMTx4 modulated pathways related to hormone level regulation, signal release, hormone transport, cellular response to biological stimuli, regulation of hormone secretion, positive regulation of adaptive immune response, and neuropeptide signaling pathways compared to the SAH

group. Additionally, Kyoto Encyclopedia of Genes and Genomes (KEGG) pathway enrichment analysis of DEGs (Fig. 7F–G) and cnetplot visualization (Fig. S10) revealed that CAQKERM@GsMTx4 influenced several key signaling pathways, including cell adhesion, the p53 signaling pathway, the NOD-like receptor signaling pathway, neuroactive ligand-receptor interactions, and cytokine-cytokine receptor interactions. These pathways align with the neuroprotective and anti-inflammatory mechanisms observed in both in vivo and in vitro studies [46]. Moreover, hierarchical clustering analysis of DEGs revealed distinct gene expression patterns across different treatment groups, highlighting molecular-level changes induced by CAQKERM@GsMTx4 (Fig. 7A).

Engineered endoplasmic reticulum membrane vesicles demonstrate excellent biosafety

Finally, the biosafety of the engineered endoplasmic reticulum membrane vesicles was thoroughly evaluated. Incucyte analysis confirmed that EV's, CAQK@EVs, and CAQKERM@EVs did not negatively impact the viability of C8-D1A, BV2, or HT22 cells (Fig. 8A), demonstrating a lack of cytotoxicity. Notably, no adverse effects were observed in the heart, liver, spleen, lungs, or kidneys of mice treated with EV's, CAQK@EVs, or CAQKERM@EVs (Fig. 8B). These results highlight the excellent biocompatibility of our engineered apolipoprotein vesicles.

Conclusion

In conclusion, our study introduces an engineered endoplasmic reticulum membrane-based nano-delivery system with targeted capabilities and enhanced cellular uptake, specifically designed for the treatment of subarachnoid hemorrhage (SAH). We demonstrated that CAQKERM@EVs exhibit exosome-like properties, including the efficient loading of the therapeutic agent GsMTx4, precise targeting of affected regions, and synergistic anti-SAH effects. These findings were validated through in vitro experiments using C8-D1A, BV2, and HT22 cells in a hemorrhagic brain injury model, as well as in vivo studies using an SAH mouse model.

Compared to traditional cell membrane-based vesicles, our engineered endoplasmic reticulum membrane vesicles displayed significantly superior cellular uptake and targeting efficiency. Specifically, CAQKERM@EVs achieved enhanced internalization in damaged C8-D1A, BV2, and HT22 cells, ensuring more effective drug delivery. Following intravenous administration, CAQKERM@EVs demonstrated exceptional targeting to hemorrhagic brain injury sites, with the highest accumulation in the brains of SAH mice. This superior performance is attributed to the unique properties of the endoplasmic reticulum membrane, which facilitates more efficient interactions with neural cell receptors and greater vesicle stability, leading to enhanced therapeutic outcomes.

Owing to these advanced targeting and uptake capabilities, CAQKERM@GsMTx4 exhibited promising therapeutic efficacy and biosafety in both in vitro and in vivo settings. The treatment effectively modulated the inflammatory immune microenvironment, reduced reactive oxygen species (ROS), promoted neuronal survival in hemorrhagic regions, and provided significant neuroprotective effects. Consequently, neurological dysfunction in SAH mice was markedly improved, as evidenced by enhanced spatial memory, learning abilities, and neurological scores. These findings underscore the potential of the engineered endoplasmic reticulum membrane-based nano-delivery system as a practical and highly effective therapeutic approach for subarachnoid hemorrhage, surpassing the performance of traditional cell membrane-based vesicles.

In summary, CAQKERM@GsMTx4, as a targeted nanodelivery system, specifically targets the brain injury region and is rapidly absorbed, demonstrating vast clinical translation potential in the field of neurosurgery. Future studies could validate its pharmacokinetics, safety, and efficacy through large animal models (such as pigs and rabbits), significantly accelerating its transition to clinical application.

Supplementary Information

The online version contains supplementary material available at https://doi.org/10.1186/s12951-025-03305-1.

Additional file 1.

Acknowledgements

This study was supported by the National Natural Science Foundation of China (81870944, F.L.). All animal experiments in this study were approved by the Animal Care and Use Committee of the Fifth Affiliated Hospital of Sun Yat-Sen University(the animal ethics approval number is:00536). Graphical abstract was created using Figdraw, and we are grateful to Home for Researchers (www.home-for-researchers.com).

Author contributions

Xiaojian Zhang: Writing—review & editing, Writing—original draft, Visualization, Validation, Software, Resources, Methodology, Investigation, Formal analysis, Data curation, Conceptualization. Enyan Jiang: Writing—original draft, Visualization, Validation, Methodology, Investigation, Formal analysis. Wangyang Fu: Validation, Software, Resources, Methodology, Investigation, Conceptualization. Yuanyuan Wang: Validation, Resources, Investigation, Conceptualization. Yiping Wang: Visualization, Validation, Software, Resources, Methodology. Zhen Fang: Visualization, Validation, Resources, Methodology, Formal analysis. Zichen Zhang: Visualization, Validation, Resources, Methodology. Jiajia Duan: Writing—review & editing,

Resources, Methodology, Formal analysis, Data curation, Conceptualization. Jia Zeng: Supervision, Resources, Funding acquisition, Conceptualization. Yang Yan: Writing—review & editing, Supervision, Resources, Validation, Funding acquisition, Conceptualization. Fei Liu: Writing—review & editing, Supervision, Resources, Project administration, Funding acquisition, Conceptualization.

Funding
This work was funded by the National Natural Science Foundation of China (Grant no. 81870944, F.L.).

Availability of data and materials
No datasets were generated or analysed during the current study. Data will be made available on request.

Declarations

Competing interests
The authors declare no competing interests.

Author details
[1]Department of Neurosurgery, The Fifth Affiliated Hospital of Sun Yat-Sen University, Zhuhai 519000, Guangdong, People's Republic of China. [2]Guangdong Provincial Engineering Research Center of Molecular Imaging, The Fifth Affiliated Hospital, Sun Yat-Sen University, Zhuhai, Guangdong, People's Republic of China. [3]Guangdong-Hong Kong-Macao University Joint of Interventional Medicine, The Fifth Affiliated Hospital, Sun Yat-Sen University, Zhuhai, Guangdong, People's Republic of China. [4]State Key Laboratory of Oncology in South China, Guangdong Provincial Clinical Research Center for Cancer, Sun Yat-Sen University Cancer Center, Guangzhou 510060, People's Republic of China. [5]Department of Medical Oncology, Sun Yat-Sen University Cancer Center, Guangzhou, People's Republic of China.

Received: 28 November 2024 Accepted: 8 March 2025
Published online: 05 April 2025

References

1. Etminan N. Aneurysmal subarachnoid hemorrhage—status quo and perspective. Transl Stroke Res. 2015;6:167–70.
2. Lublinsky S, Major S, Kola V, Horst V, Santos E, Platz J, Sakowitz O, Scheel M, Dohmen C, Graf R, Vatter H, Wolf S, Vajkoczy P, Shelef I, Woitzik J, Martus P, Dreier JP, Friedman A. Early blood-brain barrier dysfunction predicts neurological outcome following aneurysmal subarachnoid hemorrhage. EBioMedicine. 2019;43:460–72.
3. Wang J, Lin F, Zeng M, Liu M, Zheng M, Ren Y, Li S, Yang X, Chen Y, Chen X, Sessler DI, Peng Y. Intraoperative blood pressure and cardiac complications after aneurysmal subarachnoid hemorrhage: a retrospective cohort study. Int J Surg. 2024;110:965–73.
4. Li X, Zeng L, Lu X, Chen K, Yu M, Wang B, Zhao M. Early brain injury and neuroprotective treatment after aneurysmal subarachnoid hemorrhage: a literature review. Brain Sci. 2023;13:1083.
5. Higashi Y, Maruhashi T, Noma K, Kihara Y. Oxidative stress and endothelial dysfunction: clinical evidence and therapeutic implications. Trends Cardiovasc Med. 2014;24:165–9.
6. Weng W, Cheng F, Zhang J. Specific signature biomarkers highlight the potential mechanisms of circulating neutrophils in aneurysmal subarachnoid hemorrhage. Front Pharmacol. 2022;13:1022564.
7. Hoh BL, Ko NU, Amin-Hanjani S, Chou S-Y, Cruz-Flores S, Dangayach NS, Derdeyn CP, Du R, Hänggi D, Hetts SW, Ifejika NL, Johnson R, Keigher KM, Leslie-Mazwi TM, Lucke-Wold B, Rabinstein AA, Robicsek SA, Stapleton CJ, Suarez JI, Tjoumakaris SI, Welch BG. Guideline for the management of patients with aneurysmal subarachnoid hemorrhage: a guideline from the American Heart Association/American Stroke Association. Stroke. 2023;54(2023):e314–70.
8. Coste B, Mathur J, Schmidt M, Earley TJ, Ranade S, Petrus MJ, Dubin AE, Patapoutian A. Piezo1 and Piezo2 are essential components of distinct mechanically activated cation channels. Science. 2010;330:55–60.
9. Qu J, Zong HF, Shan Y, Zhang SC, Guan WP, Yang Y, Zhao HL. Piezo1 suppression reduces demyelination after intracerebral hemorrhage. Neural Regen Res. 2023;18:1750–6.
10. Zhu T, Guo J, Wu Y, Lei T, Zhu J, Chen H, Kala S, Wong KF, Cheung CP, Huang X, Zhao X, Yang M, Sun L. The mechanosensitive ion channel Piezo1 modulates the migration and immune response of microglia. iScience. 2023;26: 105993.
11. Zeng J, Fang Z, Duan J, Zhang Z, Wang Y, Wang Y, Chen L, Wang J, Liu F. Activation of Piezo1 by intracranial hypertension induced neuronal apoptosis via activating hippo pathway. CNS Neurosci Ther. 2024;30: e14872.
12. Suchyna TM. Piezo channels and GsMTx4: two milestones in our understanding of excitatory mechanosensitive channels and their role in pathology. Prog Biophys Mol Biol. 2017;130:244–53.
13. Lin Z, Xu G, Lu X, Wang H, Lu F, Xia X, Song J, Jiang J, Ma X, Zou F. Piezo1 exacerbates inflammation-induced cartilaginous endplate degeneration by activating mitochondrial fission via the Ca^{2+}/CaMKII/Drp1 axis. Aging Cell. 2024;e14440. https://doi.org/10.1111/acel.14440
14. Thien ND, Hai-Nam N, Anh DT, Baecker D. Piezo1 and its inhibitors: overview and perspectives. Eur J Med Chem. 2024;273: 116502.
15. Li Q, Li C, Li X, Liu X, Qian J, Li J, Li X, Zhang X. GsMTx4 combined with exercise exerts neuroprotective effects by regulating neuronal autophagy in rats with spinal cord injury. Neurochem Res. 2024;50:55.
16. Farhangi S, Karimi E, Khajeh K, Hosseinkhani S, Javan M. Peptide mediated targeted delivery of gold nanoparticles into the demyelination site ameliorates myelin impairment and gliosis. Nanomedicine. 2023;47: 102609.
17. Sun J, Liu J, Gao C, Zheng J, Zhang J, Ding Y, Gong W, Yang M, Li Z, Wang Y, Yang Y, Gao C. Targeted delivery of PARP inhibitors to neuronal mitochondria via biomimetic engineered nanosystems in a mouse model of traumatic brain injury. Acta Biomater. 2022;140:573–85.
18. Mann AP, Scodeller P, Hussain S, Joo J, Kwon E, Braun GB, Mölder T, She ZG, Kotamraju VR, Ranscht B, Krajewski S, Teesalu T, Bhatia S, Sailor MJ, Ruoslahti E. A peptide for targeted, systemic delivery of imaging and therapeutic compounds into acute brain injuries. Nat Commun. 2016;7:11980.
19. Yu Z, Li J, Zhu J, Zhu M, Jiang F, Zhang J, Li Z, Zhong M, Kaye JB, Du J, Shen B. A synthetic transmembrane segment derived from TRPV4 channel self-assembles into potassium-like channels to regulate vascular smooth muscle cell membrane potential. J Mater Chem B. 2014;2:3809–18.
20. Liu J, Sun Y, Zeng X, Liu Y, Liu C, Zhou Y, Liu Y, Sun G, Guo M. Engineering and characterization of an artificial drug-carrying vesicles nanoplatform for enhanced specifically targeted therapy of glioblastoma. Adv Mater. 2023;35: e2303660.
21. Bai S, Wang Z, Zhang Y, Yang Y, Wei Y, Luo Y, Wang M, Shen B, He W, Yang Z, Hui H, Du J. iRGD-TRP-PK1-modified red blood cell membrane vesicles as a new chemotherapeutic drug delivery and targeting system in head and neck cancer. Theranostics. 2025;15:86–102.
22. Liu X, Chen Y, Fu Y, Jiang D, Gao F, Tang Z, Bian X, Wu S, Yu Y, Wang X, Shen J, Li C. Breaking spatiotemporal barriers of immunogenic chemotherapy via an endoplasmic reticulum membrane-assisted liposomal drug delivery. ACS Nano. 2023;17:10521–34.
23. Qiu C, Han HH, Sun J, Zhang HT, Wei W, Cui SH, Chen X, Wang JC, Zhang Q. Regulating intracellular fate of siRNA by endoplasmic reticulum membrane-decorated hybrid nanoplexes. Nat Commun. 2019;10:2702.
24. Caceres PS, Mendez M, Haque MZ, Ortiz PA. Vesicle-associated membrane protein 3 (VAMP3) mediates constitutive trafficking of the renal co-transporter NKCC2 in thick ascending limbs: role in renal function and blood pressure. J Biol Chem. 2016;291:22063–73.
25. Ganley IG, Espinosa E, Pfeffer SR. A syntaxin 10-SNARE complex distinguishes two distinct transport routes from endosomes to the trans-Golgi in human cells. J Cell Biol. 2008;180:159–72.
26. Hsu JL, Chou JW, Chen TF, Hsu JT, Su FY, Lan JL, Wu PC, Hu CM, Lee EY, Lee WH. Glutathione peroxidase 8 negatively regulates caspase-4/11 to protect against colitis. EMBO Mol Med. 2020;12: e9386.
27. Sun H, Su J, Meng Q, Yin Q, Chen L, Gu W, Zhang P, Zhang Z, Yu H, Wang S, Li Y. Cancer-cell-biomimetic nanoparticles for targeted therapy of homotypic tumors. Adv Mater. 2016;28:9581–8.
28. Zhang T, Zhong H, Lin L, Zhang Z, Xue K, He F, Luo Y, Wang P, Zhao Z, Cong L, Pang P, Li X, Shan H, Yan Z. Core microbiome-associated proteins

associated with ulcerative colitis interact with cytokines for synergistic or antagonistic effects on gut bacteria. ISME J. 2024;18:wrae146.
29. Liu Y, Yao C, Sheng B, Zhi S, Chen X, Ding P, Zhang J, Tao Z, Li W, Zhuang Z, Mao J, Peng Z, Yan H, Jin W. Inhibition of USP30 promotes mitophagy by regulating ubiquitination of MFN2 by parkin to attenuate early brain injury after SAH. Transl Stroke Res. 2023. https://doi.org/10.1007/s12975-024-01245-w.
30. Garcia JH, Wagner S, Liu KF, Hu XJ. Neurological deficit and extent of neuronal necrosis attributable to middle cerebral artery occlusion in rats. Statistical validation. Stroke. 1995; 26:627–634; discussion 635.
31. Tsai YY, Huang YH, Chao YL, Hu KY, Chin LT, Chou SH, Hour AL, Yao YD, Tu CS, Liang YJ, Tsai CY, Wu HY, Tan SW, Chen HM. Identification of the nanogold particle-induced endoplasmic reticulum stress by omic techniques and systems biology analysis. ACS Nano. 2011;5:9354–69.
32. Clairmont CA, De Maio A, Hirschberg CB. Translocation of ATP into the lumen of rough endoplasmic reticulum-derived vesicles and its binding to luminal proteins including BiP (GRP 78) and GRP 94. J Biol Chem. 1992;267:3983–90.
33. Merkel A, Chen Y, Villani C, George A. GRP78 promotes the osteogenic and angiogenic response in periodontal ligament stem cells. Eur Cell Mater. 2023;45:14–30.
34. Lee JU, Hong J, Shin H, Ryu CB, Park SW, Jeong SH. Overexpression of V-ATPase B2 attenuates lung injury/fibrosis by stabilizing lysosomal membrane permeabilization and increasing collagen degradation. Exp Mol Med. 2022;54:662–72.
35. Ruscher K, Wieloch T. The involvement of the sigma-1 receptor in neurodegeneration and neurorestoration. J Pharmacol Sci. 2015;127:30–5.
36. Li T, Chen Y, Li Y, Yao Z, Liu W. FAM134B-mediated endoplasmic reticulum autophagy protects against sepsis myocardial injury in mice. Aging. 2021;13:13535–47.
37. Yang Z, Wang J, He B, Zhang X, Li X, Kuang E. RTN3 inhibits RIG-I-mediated antiviral responses by impairing TRIM25-mediated K63-linked polyubiquitination. Elife. 2021;10: e68958.
38. Yu W, Yin N, Yang Y, Xuan C, Liu X, Liu W, Zhang Z, Zhang K, Liu J, Shi J. Rescuing ischemic stroke by biomimetic nanovesicles through accelerated thrombolysis and sequential ischemia-reperfusion protection. Acta Biomater. 2022;140:625–640. https://doi.org/10.1016/j.actbio.2021.12.009
39. Hase Y, Craggs L, Hase M, Stevenson W, Slade J, Lopez D, Mehta R, Chen A, Liang D, Oakley A, Ihara M, Horsburgh K, Kalaria RN. Effects of environmental enrichment on white matter glial responses in a mouse model of chronic cerebral hypoperfusion. J Neuroinflammation. 2017;14:81.
40. Wakita H, Tomimoto H, Akiguchi I, Kimura J. Glial activation and white matter changes in the rat brain induced by chronic cerebral hypoperfusion: an immunohistochemical study. Acta Neuropathol. 1994;87:484–92.
41. Zhao Y, Zhang J, Zheng Y, Zhang Y, Zhang XJ, Wang H, Du Y, Guan J, Wang X, Fu J. NAD^+ improves cognitive function and reduces neuroinflammation by ameliorating mitochondrial damage and decreasing ROS production in chronic cerebral hypoperfusion models through Sirt1/PGC-1α pathway. J Neuroinflammation. 2021;18:207.
42. Nam HY, Nam JH, Yoon G, Lee JY, Nam Y, Kang HJ, Cho HJ, Kim J, Hoe HS. Ibrutinib suppresses LPS-induced neuroinflammatory responses in BV2 microglial cells and wild-type mice. J Neuroinflammation. 2018;15:271.
43. Hannemann N, Cao S, Eriksson D, Schnelzer A, Jordan J, Eberhardt M, Schleicher U, Rech J, Ramming A, Uebe S, Ekici A, Cañete JD, Chen X, Bäuerle T, Vera J, Bogdan C, Schett G, Bozec A. Transcription factor Fra-1 targets arginase-1 to enhance macrophage-mediated inflammation in arthritis. J Clin Invest. 2019;129:2669–84.
44. Linnerbauer M, Wheeler MA, Quintana FJ. Astrocyte crosstalk in CNS inflammation. Neuron. 2020;108:608–22.
45. Vismara I, Papa S, Veneruso V, Mauri E, Mariani A, De Paola M, Affatato R, Rossetti A, Sponchioni M, Moscatelli D, Sacchetti A, Rossi F, Forloni G, Veglianese P. Selective modulation of A1 astrocytes by drug-loaded nano-structured gel in spinal cord injury. ACS Nano. 2020;14:360–71.
46. Zhou X, Deng X, Liu M, He M, Long W, Xu Z, Zhang K, Liu T, So KF, Fu QL, Zhou L. Intranasal delivery of BDNF-loaded small extracellular vesicles for cerebral ischemia therapy. J Control Release. 2023;357:1–19.

Publisher's Note